Defining the rate-limiting processes of bacterial cytokinesis

Carla Coltharp[a], Jackson Buss[a,1], Trevor M. Plumer[a], and Jie Xiao[a,2]

[a]Department of Biophysics and Biophysical Chemistry, Johns Hopkins University School of Medicine, Baltimore, MD 21205

Edited by Joe Lutkenhaus, University of Kansas Medical Center, Kansas City, KS, and approved January 6, 2016 (received for review July 22, 2015)

Bacterial cytokinesis is accomplished by the essential 'divisome' machinery. The most widely conserved divisome component, FtsZ, is a tubulin homolog that polymerizes into the 'FtsZ-ring' ('Z-ring'). Previous in vitro studies suggest that Z-ring contraction serves as a major constrictive force generator to limit the progression of cytokinesis. Here, we applied quantitative superresolution imaging to examine whether and how Z-ring contraction limits the rate of septum closure during cytokinesis in *Escherichia coli* cells. Surprisingly, septum closure rate was robust to substantial changes in all Z-ring properties proposed to be coupled to force generation: FtsZ's GTPase activity, Z-ring density, and the timing of Z-ring assembly and disassembly. Instead, the rate was limited by the activity of an essential cell wall synthesis enzyme and further modulated by a physical divisome–chromosome coupling. These results challenge a Z-ring–centric view of bacterial cytokinesis and identify cell wall synthesis and chromosome segregation as limiting processes of cytokinesis.

FtsZ | superresolution | force generation | cytokinesis | cell wall synthesis

The mechanisms that drive bacterial cell division have been sought out for many decades because of their essential role in bacterial proliferation and their appeal as targets for new antibiotic development (1). Numerous cellular and biochemical investigations have revealed that bacterial cytokinesis is carried out by a dynamic, supramolecular complex termed the 'divisome.' The divisome assembles at midcell to coordinate constriction of the multilayer cell envelope (2), which involves both membrane invagination and new septal cell wall synthesis.

Divisome assembly is initiated by the highly-conserved tubulin-like GTPase FtsZ (3, 4). FtsZ's membrane tethers [FtsA and ZipA in *Escherichia coli* (5, 6)] promote FtsZ's polymerization into a ring-like structure, or 'FtsZ-ring' ('Z-ring'), at the cytoplasmic face of the inner membrane (7). Once established, the Z-ring recruits an ensemble of transmembrane and periplasmic proteins involved in cell wall peptidoglycan (PG) synthesis and remodeling, including the essential transpeptidase and penicillin-binding protein PBP3 (also called FtsI) (8, 9). Recently, a new group of Z-ring–associated proteins (Zaps) has been shown to stabilize the Z-ring (10–15). Some of these Zaps connect the Z-ring to the bacterial chromosome through a multilayered protein network that includes the chromosome-binding protein MatP (16–19). Together with FtsK, a divisome protein involved in chromosome segregation and dimer resolution (20–25), this group of proteins likely plays a role in coordinating cell envelope invagination with chromosome segregation (16, 18, 26). Thus, the divisome consists of three interacting components: the Z-ring, PG-linked proteins, and chromosome-linked proteins.

Successful cell constriction requires a mechanical force to act against the internal turgor pressure. However, the divisome component responsible for generating such a force remains unclear (27). One possibility that has garnered much attention in the last decade is a 'Z-ring–centric' model in which the Z-ring is analogous to the contractile actomyosin ring in eukaryotic cells: the Z-ring is thought to actively pull the cytoplasmic membrane inward, and septal PG growth follows passively behind (28). Such a model predicts that Z-ring contraction limits the progression of septum closure and is distinct from a model in which new septal PG growth actively pushes from the outside of the cytoplasmic membrane (27). In this latter model, PG synthesis limits the rate of septum closure, and the Z-ring acts as a scaffold that passively follows the closing septum (29). Alternatively, Z-ring contraction and septal cell wall synthesis may work together to drive constriction; in which case, progression of septum closure would be regulated by both processes (27).

A large number of studies support the Z-ring–centric force generation model. For example, purified, membrane-tethered FtsZ was shown to assemble into ring-like structures that deform and constrict liposome membranes (30–35). Mechanistically, it has been proposed that a constrictive force could be generated by the bending of FtsZ protofilaments because of their preferred curvature or GTP hydrolysis-induced conformation change (36–41), immediate reannealing of FtsZ protofilaments upon GTP hydrolysis-induced subunit loss (42), condensation of FtsZ protofilaments caused by their lateral affinity (43), or a combination of these mechanisms (38, 42, 44, 45). However, these proposed mechanisms have been difficult to test in vivo because of the essentiality of FtsZ, the limited ability to spatially resolve the Z-ring structure in small bacterial cells, and the lack of sensitive methods to monitor Z-ring contraction and the rate of septum closure.

In this work, we applied quantitative superresolution imaging in combination with other biophysical techniques to characterize Z-ring structure and dynamics during constriction and to probe the rate of septum closure during cell constriction. We reasoned that perturbations to the structure or activity of the major force-generating divisome component should result in significant changes

Significance

Bacterial cytokinesis is orchestrated by a macromolecular complex termed the divisome. Central to the divisome is a ring-like, polymeric structure, called the FtsZ-ring (Z-ring). The Z-ring may generate a constrictive force analogous to that provided by the eukaryotic actomyosin ring to drive membrane invagination during cytokinesis. By combining single-molecule imaging with genetic manipulations, we found that, unexpectedly, the rate of septum closure in *Escherichia coli* cells during cytokinesis is robust to many substantial Z-ring perturbations but limited by a specific cell wall synthesis enzyme and further modulated by a physical link between the divisome and chromosome. Our results challenge the long-held Z-ring–centric view of bacterial cytokinesis and support a holistic view of constrictive force generation by the multicomponent divisome.

Author contributions: C.C., J.B., and J.X. designed research; C.C., J.B., and T.M.P. performed research; C.C., J.B., and J.X. contributed new reagents/analytic tools; C.C., T.M.P., and J.X. analyzed data; and C.C. and J.X. wrote the paper.

The authors declare no conflict of interest.

[1]Present address: Department of Microbiology and Immunobiology, Harvard Medical School, Boston, MA 02115.

[2]To whom correspondence should be addressed. Email: xiao@jhmi.edu.

This article contains supporting information online at www.pnas.org/lookup/suppl/doi:10.1073/pnas.1514296113/-/DCSupplemental.

to the rate of septum closure, allowing us to identify possible molecular mechanisms for constriction force generation.

Surprisingly, we found that the rate of septum closure was unaffected by many substantial alterations to the Z-ring, including FtsZ's GTPase activity, molecular density of the Z-ring, and the timing of Z-ring assembly and disassembly. Instead, the rate of septum closure was proportional to the rate of cell elongation and was significantly reduced when FtsI activity was compromised, indicating that cell wall synthesis plays a limiting role in septum closure. Interestingly, we found that deletion of *matP* caused the septum to close faster than predicted by the corresponding cell elongation rate, indicating that the coordination of cell envelope invagination with chromosome segregation by MatP can influence the progression of cell constriction.

Taken together, our results challenge the FtsZ-centric view of bacterial cytokinesis, highlight the role of septal cell wall growth and chromosome segregation in driving and modulating the rate of septum closure, and support a holistic view of constrictive force generation by the multicomponent divisome.

Results

Three-Dimensional Structure of the *E. coli* Z-Ring During Constriction. Proposed Z-ring force generation models predict that Z-ring structure would be remodeled in different ways as it contracts [i.e., thickening (46), widening (44), condensing (43), or disassembling (38, 39, 42)]. To determine whether the Z-ring undergoes such structural remodeling in vivo, we examined Z-ring structures using the single-molecule–based superresolution technique, photoactivated localization microscopy (PALM) (47). Previously, we conducted 2D PALM imaging of the *E. coli* Z-ring using a photoactivatable fluorescent protein fusion FtsZ-mEos2 (18, 19, 48–50). We showed that the Z-ring is not a smooth structure but instead comprises clusters of FtsZ protofilaments that loosely associate into a 3D bundle (19, 48). This heterogeneous morphology has also been observed with several different fluorescent protein tags (19), in different bacterial species (51–54), by immuno-superresolution imaging targeting native FtsZ (19, 54), by superresolution imaging of FtsZ-binding proteins (19, 54), and in an early electron cryotomography (ECT) study (37). Here, we further demonstrate that an FtsZ-GFP fusion colocalizes with native FtsZ in midcell clusters in two-color superresolution imaging using antibodies against native FtsZ and GFP (*SI Appendix*, Fig. S1). These results suggest that the cluster-like organization of the Z-ring is not caused by fluorescent protein fusion but is likely an intrinsic property of FtsZ polymerization and dynamics in vivo (*Discussion*).

To provide a nanoscale characterization of the Z-ring structure in 3D, we applied interferometric PALM (iPALM) imaging (18, 55) to *E. coli* Z-rings labeled with FtsZ-mEos2. iPALM identifies a molecule's z position using the interference of the molecule's emitted light along two optical paths and provides the best z resolution currently available to fluorescence-based superresolution imaging (56). Under our experimental condition using the mEos2 fusion protein, we achieved spatial resolutions of ∼30 nm, ∼24 nm, and ∼16 nm in the x, y, and z dimensions, respectively (*SI Appendix*, Fig. S2 and Table S1).

Fig. 1 shows representative iPALM images of fixed *E. coli* cells (strains BW25113 and DH5α) ectopically expressing FtsZ-mEos2. These images highlight the punctate structure of the Z-ring, which is normally blurred into a smooth ring when viewed under a conventional fluorescence microscope (19, 48). This punctate Z-ring morphology was observed at different FtsZ-mEos2 expression levels and with sufficiently high labeling density required by the Nyquist resolution (*Materials and Methods* and *SI Appendix*, Fig. S3*A*). Interestingly, we often observed non-midcell clusters of FtsZ-mEos2 (Fig. 1*A*, white and cyan arrows), which may be related to the longitudinally oscillating and periodic FtsZ structures observed previously (57, 58). Some non-midcell clusters are clearly displaced from the membrane (Fig. 1*A*, cyan arrows), suggesting that FtsZ can polymerize in the absence of its membrane tethers in the cytoplasm.

Cross-sectional projections of FtsZ-mEos2 clusters in the Z-ring (Fig. 1*B*) show that FtsZ clusters are confined to a toroidal zone. The apparent width and thickness of this zone (see measurement example in *SI Appendix*, Fig. S4) were similar in the two *E. coli* strains (*SI Appendix*, Table S1). The combined mean Z-ring width (along the cell long axis) of 99 ± 3 nm (n = 168; Fig. 1*C*) is consistent with previous measurements of 60–120 nm in *E. coli* (19, 48, 59) and *Caulobacter crescentus* (53, 60). Note that dimension measurements reported here have been deconvolved from the achieved resolution to facilitate comparison across different experiments (61) (*Materials and Methods*); see *SI Appendix*, Table S1 for apparent dimensions before deconvolution. The mean Z-ring thickness in the radial direction was significantly smaller than the width (59 ± 2 nm, $P < 1 \times 10^{-29}$, n = 168; Fig. 1*C*) but larger than the expected size of a single protofilament layer

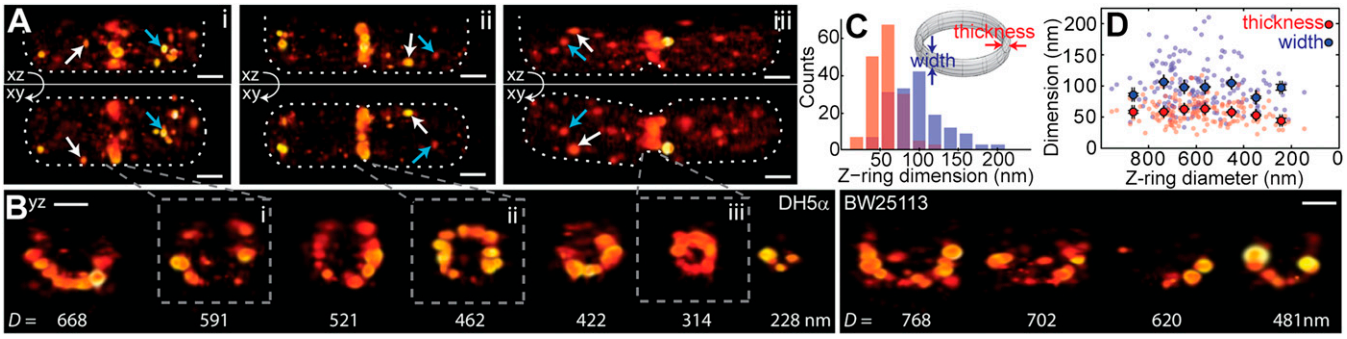

Fig. 1. The *E. coli* Z-ring in 3D. (*A*) Two-dimensional projections of iPALM images of three fixed *E. coli* DH5α cells expressing FtsZ-mEos2. (*A*, *Upper*) *xz* plane. (*A*, *Lower*) *xy* plane. Arrows illustrate cytoplasmic (cyan) and membrane-proximal (white) clusters of FtsZ-mEos2 outside the Z-ring. Cell outlines are approximated by white dotted lines. (*B*) Cropped midcell regions of DH5α (*Left*) and BW25113 (*Right*) cells showing Z-rings projected on *yz* planes. Fitted ring diameters are shown below each Z-ring. Rings outlined in dashed boxes correspond to those shown in *A*. (*C*) Distributions of resolution-deconvolved Z-ring cross-sectional width (blue) and thickness (red) measured from iPALM images of FtsZ-mEos2 in DH5α and BW25113 cells (n = 168). Each histogram bin width is 20 nm. The inset schematic shows the relative orientations of Z-ring thickness (along the cell radius) and Z-ring width (along the cell long axis). (*D*) Resolution-deconvolved Z-ring width (blue) and thickness (red) plotted against corresponding Z-ring diameter (n = 168). Measurements for individual cells are shown as small, transparent, filled circles. Average measurements for cells binned by ring diameter (bin edges: 0, 300, 400, 500, 600, 700, 800, and 1,000 nm) are shown as larger filled circles with black outlines. Error bars represent SEM. The image axes are as follows: x axis, cell long axis; y axis, cell short axis parallel to the imaging plane; and z axis, cell short axis perpendicular to the imaging plane. (Scale bars, 300 nm.)

(~5 nm; would appear as ~30 nm under our resolution). This direct measurement indicates that the Z-ring can accommodate multiple layers of FtsZ protofilaments along the radial direction of the cell.

To characterize the size and distribution of FtsZ clusters, we performed autocorrelation and density histogram analyses (*SI Appendix*, *Supplemental Experimental Procedures*) (61–63) of FtsZ clusters projected along the Z-ring's circumference. These distributions were well described by a model in which, on average, 10–20 FtsZ clusters (μm^{-1}) of 30- to 50-nm length (FWHM) are randomly distributed along the Z-ring (*SI Appendix*, Fig. S5). Confinement of these clusters to a ~60 × 100 nm Z-ring cross-section in vivo (*SI Appendix*, Table S1) indicates that FtsZ protofilaments in Z-ring clusters typically do not grow longer than 100 nm in any direction, which is within the 100- to 200-nm range of protofilament lengths observed in vitro (64–66) and consistent with random orientations of FtsZ protofilaments in the Z-ring (67).

Z-Ring Architecture Does Not Undergo Substantial Remodeling During Constriction. To investigate possible structural remodeling of the Z-ring during constriction, we next generated a pseudo–time-lapse sequence by arranging individual Z-rings according to their diameters (representative images are shown in Fig. 1*B*). Qualitative inspection showed that the Z-ring remained heterogeneous and discontinuous throughout constriction and that the ring cross-section did not appreciably expand or decrease in size. Plotting measured Z-ring cross-sectional dimensions against the corresponding ring diameters of individual cells confirmed that both Z-ring width and thickness remained largely constant (Fig. 1*D*).

To assess whether the trend we observed was representative of native, unlabeled FtsZ, we also performed a similar analysis on ring structures formed by ZapA, using ectopic expression of an mEos2-ZapA fusion protein that can rescue the elongated cell phenotype of a *zapA* null mutant (18). ZapA binds to FtsZ to promote Z-ring assembly (10, 68) and has been used as a marker for FtsZ localization and dynamics (69, 70). iPALM images of mEos2-ZapA in BW25113 cells showed punctate structures similar to those of FtsZ-mEos2 (*SI Appendix*, Fig. S6*A*) (18). The mEos2-ZapA clusters were confined to a slightly smaller zone than FtsZ-mEos2 (mean width of 85 ± 4 nm and thickness of 46 ± 3 nm, $n = 43$; *SI Appendix*, Table S1 and Fig. S6*B*). Importantly, no significant changes in either the width or thickness of ZapA-rings were observed across cells of different diameters (*SI Appendix*, Fig. S6*C*), supporting our observation that the Z-ring cross-sectional dimensions remain constant throughout constriction. Thus, if the Z-ring does generate a constrictive force in vivo, the force is unlikely to involve ring thickening or widening as some models have proposed (44, 46).

Constriction Initiation and Progress Does Not Require Z-Ring Disassembly. To investigate whether Z-ring assembly or disassembly were coupled to the progression of cell constriction, we used time-lapse fluorescence imaging of dividing BW25113 cells expressing FtsZ-GFP growing in M9 minimal medium at room temperature (RT) (Fig. 2*A* and *SI Appendix*, Table S2). Fig. 2*A* shows a representative montage of FtsZ-GFP assembly and disassembly dynamics, which are quantified in Fig. 2*B* as the percentage of FtsZ-GFP localized to the midcell (p_{mid}) plotted against cell cycle time (t). This percentage value normalizes for differences in FtsZ expression levels among individual cells, because it is unaffected by overexpression of up to eightfold the endogenous FtsZ level (48). The p_{mid} values are also indicative of the amount of FtsZ in the Z-ring at different cell cycle stages (48, 71, 72), because the concentration of FtsZ throughout the cell cycle is constant (73, 74).

The time-lapse behavior of FtsZ-GFP (Fig. 2*B*) was consistent with previous observations (28, 75, 76) showing that Z-ring dynamics can be divided into three cell-cycle periods: Z-ring assembly (the time between cell birth and stabilization of the Z-ring at midcell), Z-ring maintenance (during which Z-ring intensity remains largely constant), and Z-ring disassembly (during which Z-ring intensity decreases, concluded by daughter cell separation) (Fig. 2*C*). We note that the bulk Z-ring assembly and disassembly described here on the cell cycle timescale is different from the constant FtsZ subunit turnover process that occurs on the seconds timescale (71, 72). Interestingly, corresponding bright-field images revealed that visible indentation of the cell wall (arrow iii in Fig. 2*A*) did not coincide with the initiation of Z-ring disassembly (arrow iv in Fig. 2*A*) but preceded Z-ring disassembly significantly (by 35 ± 2 min; Fig. 2*C* and *SI Appendix*, Table S2). Note that this delay may be even longer as septum indentation initiates earlier than we can detect with diffraction-limited bright field microscopy (77). The duration of visible cell constriction, τ_c, can thus be divided into phase I (from the first visible cell wall indentation to the initiation of Z-ring disassembly) and phase II (Z-ring disassembly). The substantial duration of constriction phase I suggests that, although theoretical models suggest that Z-ring disassembly can drive constriction (38, 39, 42), constriction can both initiate and proceed without Z-ring disassembly in vivo.

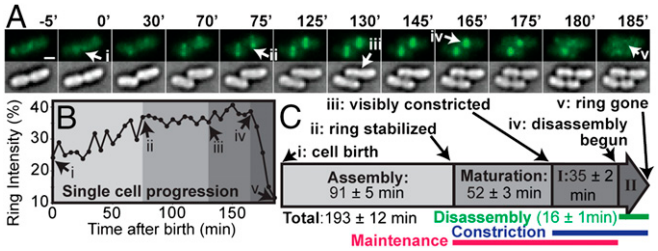

Fig. 2. Time-lapse analysis of Z-ring dynamics during the cell cycle. (*A*) Time-lapse fluorescence (*Upper*) and bright-field (*Lower*) montage of BW25113 cells expressing FtsZ-GFP. Arrows indicate cell cycle landmarks for the top cell: arrow i, cell birth; arrow ii, ring stabilization; arrow iii, onset of visible constriction; arrow iv, beginning of Z-ring disassembly; and arrow v, completion of cell division. The time stamp (*Upper Right*) is displayed as minutes relative to cell birth. (*B*) Time-dependent Z-ring fluorescence (percentage of fluorescence in the ring relative to that of the whole cell, p_{mid}) during the cell cycle of the top cell shown in *A*. (C) Averaged durations of each cell cycle period for BW25113 cells growing in M9 medium at RT (means ± SE; $n = 98$). (Scale bar, 1 μm.)

The Z-Ring Condenses Throughout Constriction. The observation that cell wall indentation begins before Z-ring disassembly suggests that Z-ring density (i.e., FtsZ concentration in the ring) likely increases during constriction phase I. Such Z-ring condensation, caused by favorable lateral interactions between FtsZ protofilaments, is theoretically capable of providing a mechanical force to drive constriction (43). To directly assess the extent of Z-ring condensation during constriction, we next performed live 2D PALM imaging to compare Z-ring densities at different constriction stages.

PALM images of live, constricting BW25113 cells expressing FtsZ-mEos2 revealed similar discontinuous, heterogeneous Z-ring morphologies and dimensions throughout cytokinesis (Fig. 3 *C* and *E* and *SI Appendix*, Table S1) and varying expression levels (*SI Appendix*, Fig. S3*B*), analogous to those observed in fixed-cell iPALM images (Fig. 1 *A* and *B* and *SI Appendix*, Fig. S3*A*). The midcell percentage (p_{mid}) of FtsZ-mEos2 remained constant until the Z-ring diameter reached ~250 nm (Fig. 3*F*), consistent with previous studies that monitored early stages of Z-ring closure (diameter, >300 nm) (43, 51). However, in cells with smaller diameters (<250 nm), p_{mid} decreased significantly (Fig. 3*F*). These results are consistent with the two-phase constriction identified by

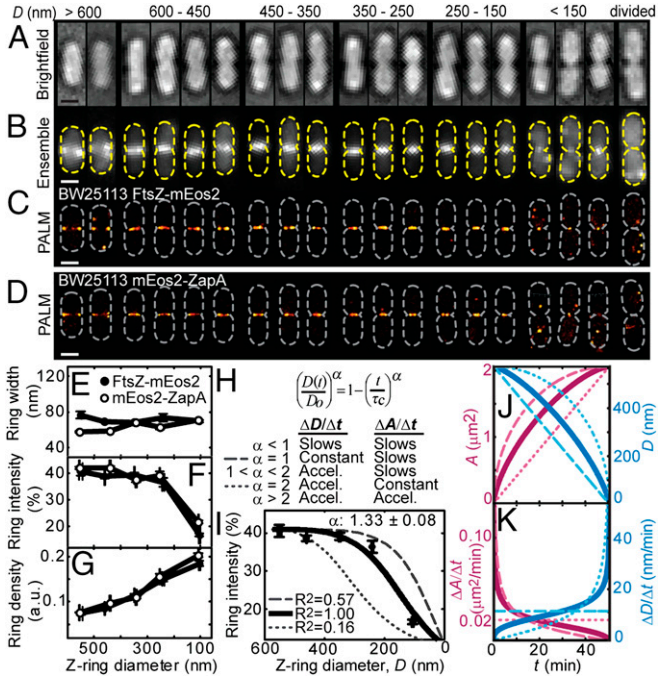

Fig. 3. Analysis of Z-ring remodeling during constriction and time-dependent septum closure rate for BW25113 cells. (*A–C*) Bright-field (*A*), conventional green fluorescence (*B*), and superresolution PALM (*C*) images of live BW25113 cells expressing FtsZ-mEos2 grouped by measured Z-ring diameter. Cell outlines are approximated by dashed lines. (*D*) PALM images of live BW25113 cells expressing mEos2-ZapA grouped by ring diameter as in *C*. (*E–G*) Resolution-deconvolved ring width (*E*), intensity (p_{mid}) (*F*), and density (*G*) in BW25113 cells expressing FtsZ-mEos2 (filled; $n = 66$) or mEos2-ZapA (empty; $n = 82$) plotted against and binned by corresponding ring diameter. Bin edges are as follows: 0, 200, 300, 400, 500, and 600 nm. Errors bars represent SEM. (*H*) Equation describing the monotonic decrease in Z-ring diameter over time (*Upper*) and table describing different α regimes for the rates of septum diameter closure, $\Delta D/\Delta t$, and septum surface area addition, $\Delta A/\Delta t$ (*Lower*). (*I*) Z-ring intensity, p_{mid}, plotted against ring diameter as in *F* overlaid with best-fit (solid black; $\alpha = 1.3 \pm 0.1$), $\alpha = 1$ (dashed gray), and $\alpha = 2$ (dotted gray) models generated from time-lapse parameters of BW25113 cells (*SI Appendix*, Table S2) using the model in *H*. The best-fit model is consistent with acceleration in septum closure rate. (*J* and *K*) Time-dependent change in septum area [$A(t)$] (*J*, magenta), septum diameter [$D(t)$] (*J*, cyan), rate of septum area addition ($\Delta A/\Delta t$) (*K*, magenta), and rate of septum diameter closure ($\Delta D/\Delta t$) (*K*, cyan) for the models shown in *I*, assuming that growing septa resemble hemispherical segments and using an average septum closure time of 51 min (*SI Appendix*, Table S2): best fit (solid), $\alpha = 1$ (dashed), and $\alpha = 2$ (dotted). (Scale bars, 1 μm.)

time-lapse imaging (Fig. 2*B*) and suggest that the Z-ring begins to disassemble when its diameter reaches ∼250 nm under this condition.

We calculated the relative density of each ring by dividing the p_{mid} value of each ring by its corresponding Z-ring diameter, which is proportional to Z-ring volume because of the largely constant ring width and thickness (Fig. 1*D*). Across the population of constricting BW25113 cells, Z-ring density increased with decreasing Z-ring diameter, reaching up to ∼2.5-fold its initial value (Fig. 3*G*), even during Z-ring disassembly (constriction phase II) at the end of cell cycle (Fig. 3*F*). Identical behavior was also observed in the absence of fluorescently labeled FtsZ using the mEos2-ZapA construct in the same BW25113 strain (Fig. 3 *D*, *F*, and *G*, empty circles), suggesting that the endogenous, unlabeled Z-ring behaves similarly to FtsZ-mEos2. Thus, the Z-ring condenses throughout both phases of constriction.

Measuring Septum Closure Rate. To assess whether any of the observed Z-ring behaviors limit constriction progression, we next established methods to measure the rate of septum closure (v_c) during the period of visible constriction (τ_c). We defined v_c as the change in Z-ring diameter, ΔD, divided by τ_c, because the membrane-associated Z-ring diameter should closely reflect septum diameter at all times and the Z-ring only leaves at the end of the constriction when the Z-ring's diameter is below our spatial resolution (see *SI Appendix, Supplemental Experimental Procedures*). The diameter at the beginning of visible constriction, D_0, was measured from PALM images of cells identified to be at the onset of visible constriction in bright field images. For BW25113 cells in M9 medium at RT, $D_0 = 578 \pm 27$ nm ($n = 13$; *SI Appendix*, Table S3). Because the septum is completely closed ($D = 0$) at the end of constriction, the time-averaged septum closure rate, v_c, was calculated to be $D_0/\tau_c = 12.5 \pm 0.4$ nm/min ($n = 98$).

We next examined whether the rate of septum closure changes during constriction. Previous attempts to measure time-dependent changes in septum closure rates produced mixed results, likely because different stages of the constriction process were examined (78, 79). Using PALM, we could not measure the time dependence of septum closure rate directly because prolonged imaging of the same cell leads to phototoxicity and is thus unreliable. To circumvent this problem, we took advantage of the fact that we measured the same quantity, the midcell localization percentage of labeled FtsZ (p_{mid}), against two different experimental axes: time (t) (Fig. 2*B*) and septum diameter (D) (Fig. 3*F*). These two datasets are related by the time-dependent change in septum diameter $D(t)$, which can be described by a generic, monotonic septum closure model:

$$\left(\frac{D(t)}{D_0}\right)^{\alpha} = 1 - \left(\frac{t}{\tau_c}\right)^{\alpha}. \qquad [1]$$

In this model, D_0 is the diameter at apparent constriction onset, τ_c is the duration of visible constriction, and t is the time elapsed since the onset of visible constriction. The exponent variable, α, reflects the change in closure rate over time, with $\alpha = 1$ corresponding to a constant closure rate (Fig. 3 *H–K*, dashed curves), $\alpha < 1$ indicating rate deceleration, and $\alpha > 1$ indicating rate acceleration.

To increase the sample size for comparison, we simulated thousands of time-lapse p_{mid} vs. t traces using the experimental distributions of constriction phase I and II durations (*SI Appendix*, Fig. S7*A*). Next, these traces were converted to p_{mid} vs. D plots using Eq. **1** and varying values of α (*SI Appendix*, Fig. S7*B*). These simulated p_{mid} vs. D plots at each α value were then averaged for least squares fitting to the experimental p_{mid} vs. D data from PALM measurements (Fig. 3*I*, circles). For BW25113 cells under this condition (RT and M9 medium), the ensemble PALM data were best described by an α value of 1.3 ± 0.1 (Fig. 3 *I–K*, solid curves), indicating that, on average, septum closure accelerates in these cells. Additionally, the hemispherical geometry of the growing septum in wild-type (wt) *E. coli* dictates that an α value of <2 corresponds to deceleration in the growth of septal surface area during constriction (78). Therefore, in wt BW25113 grown in M9 at RT, the rate of septum diameter closure during constriction accelerates, whereas the addition of septum surface area per unit time gradually decreases.

Ninety Percent Reduction in FtsZ GTPase Activity Alters Z-Ring Density and Dynamics but Not Septum Closure Rate. Having established methods to measure septum closure rates, we next investigated whether the average rate would be altered under perturbed Z-ring properties, which would be expected if Z-ring contraction drives septum closure. We first examined the effects of reduced

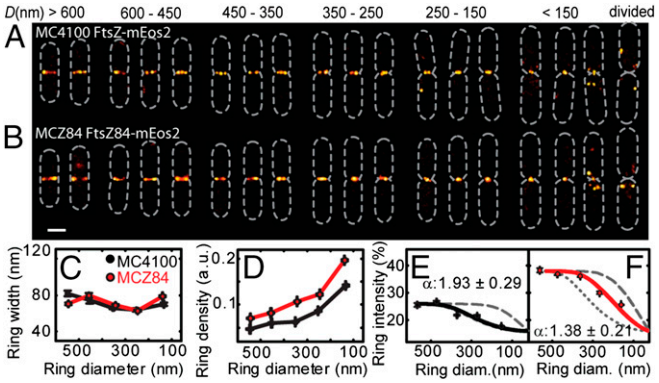

Fig. 4. Analysis of Z-ring remodeling during constriction and time-dependent septum closure rate for MC4100 and MCZ84 cells. (*A* and *B*) Superresolution PALM images of live MC4100 (*A*) and MCZ84 (*B*) cells expressing FtsZ-mEos2 or FtsZ84-mEos2, respectively, grouped by measured Z-ring diameter. Cell outlines are approximated by dashed lines. (*C*–*F*) Resolution-deconvolved ring width (*C*), density (*D*), and intensity (p_{mid}) (*E* and *F*) in MC4100 (black; $n = 83$) and MCZ84 (red; $n = 154$) cells expressing FtsZ-mEos2 or FtsZ84-mEos2, respectively, plotted against and binned by corresponding ring diameter. Bin edges are as follows: 0, 200, 300, 400, 500, and 600 nm. Errors bars represent SEM. Z-ring intensity measurements of FtsZ-mEos2 in MC4100 (*E*) and FtsZ84-mEos2 in MCZ84 (*F*) are overlaid with best fit (solid), $\alpha = 1$ (dashed gray), and $\alpha = 2$ (dotted gray) using the models in Fig. 3*H* and corresponding time-lapse parameters (*SI Appendix*, Table S2). (Scale bar, 1 μm.)

FtsZ GTPase activity, because GTP hydrolysis-dependent FtsZ protofilament bending and/or disassembly have been prominent hypotheses for force generation by the Z-ring (38, 39, 42).

We used a mutant strain, MCZ84, which expresses an FtsZ variant (FtsZ84) from the native *ftsZ* locus (80). The G105S mutation of FtsZ84 confers a ∼90% reduction in GTPase activity (3, 4, 81). Using live-cell PALM imaging of an FtsZ84-mEos2 fusion protein expressed in MCZ84, we found that the morphology and dimension of FtsZ84-rings were generally similar to those of its wt parent strain, MC4100 (Fig. 4 *A*–*C* and *SI Appendix*, Fig. S3*D*). However, consistent with previous observations (82), FtsZ84-rings exhibited higher percentages of FtsZ84-mEos2 at midcell (Fig. 4 *E* and *F* and *SI Appendix*, Fig. S3*E*), thus resulting in higher ring densities throughout constriction (Fig. 4*D* and *SI Appendix*, Fig. S3*F*).

Time-lapse analyses revealed that FtsZ84-GFP took significantly longer to stabilize at midcell in MCZ84 than wt FtsZ-GFP in MC4100 (66 ± 5 min, $n = 77$ vs. 51 ± 3 min, $n = 78$ for wt, $P = 0.01$; *SI Appendix*, Table S2). However, the average septum closure rates measured in MCZ84 and MC4100 strains were not significantly different from each other (18.0 ± 0.7 nm/min for MCZ84 and 19.3 ± 0.7 nm/min for MC4100, respectively; $P = 0.34$). Furthermore, septum closure rates accelerate in both strains, although to different degrees ($\alpha = 1.4 \pm 0.2$ vs. 1.9 ± 0.3 for MCZ84 and MC4100, respectively; Fig. 4 *E* and *F*). These results suggest that the GTPase activity of FtsZ influences Z-ring assembly and density but does not alter the time-averaged rate of septum closure significantly. Thus, the GTPase activity of FtsZ most likely does not play a limiting role in septum closure.

***minC* and *matP* Deletions Alter Z-Ring Density and Dynamics Similarly but Septum Closure Rate Differently.** We next perturbed the Z-ring by removing either MinC, a negative regulator of FtsZ polymerization, or MatP, a positive Z-ring assembly regulator. In *E. coli*, MinC oscillates between the cell poles to prevent aberrant, polar Z-ring formation (83–87). MatP is a DNA-binding protein involved in proper chromosome segregation (16, 17, 21) that stabilizes Z-ring positioning at midcell through MatP's interaction with ZapA and ZapB (18, 19, 26). We reasoned that the higher tendency of FtsZ to polymerize at places other than midcell in the absence of MinC or MatP would alter Z-ring density and the timescale of Z-ring assembly or disassembly, allowing us to assess the influence of these properties on the rate of septum closure.

We examined Z-ring structures and dynamics during the cell cycle in two BW25113 deletion mutants, Δ*minC* or Δ*matP*, using the FtsZ-mEos2 or FtsZ-GFP fusions. We found that, as expected, PALM images of FtsZ-mEos2 in Δ*minC* cells (Fig. 5*A*) often showed non-midcell FtsZ clusters, consistent with the role of MinC in preventing polar Z-ring formation (88). The Z-ring also took longer to stably assemble at midcell (108 ± 7 min, $n = 45$ vs. 91 ± 5 min, $n = 98$ for wt BW25113; $P = 0.01$). Interestingly, the effects of *matP* deletion on Z-ring morphology (Fig. 5*B*) and assembly time (114 ± 10 min, $n = 37$, $P = 0.01$ compared with wt BW25113) were remarkably similar to those of *minC* deletion.

Further analysis revealed that, in both mutants, Z-ring width remained similar to wt (Fig. 5*C* and *SI Appendix*, Fig. S3*D*), but relative Z-ring density was reduced by 20–40% compared with wt cells (Fig. 5*D* and *SI Appendix*, Fig. S3*F*). Furthermore, the Z-ring began to disassemble at larger diameters in the absence of either MinC or MatP than in the wt BW25113 parental strain (Fig. 5 *E* and *F*), but the final departure of FtsZ-GFP still coincided well with the end of constriction identified by the corresponding phase contrast images (*SI Appendix*, Fig. S8*F*). These results suggest that Z-ring disassembly is not triggered by a specific septum diameter. Surprisingly, despite producing these similar effects on Z-ring structure and assembly dynamics, the two mutations had opposing effects on septum closure rate: Δ*minC* cells exhibited slower rates ($v_c = 10.2 \pm 0.6$ nm/min) compared with wt BW25113 cells ($v_c = 12.5 \pm 0.4$ nm/min, $P = 0.004$), whereas Δ*matP* cells exhibited higher rates ($v_c = 14.2 \pm 0.9$ nm/min, $P = 0.02$ compared with wt BW25113). The elevated septum closure rate of Δ*matP* supports our previous interpretation that a shortened constriction period, τ_c, in Δ*matP* reflected a faster constriction rate relative to wt, not simply a decrease in cell diameter (18). Taken together, the opposite changes to septum closure rate caused by deletion of *matP* or *minC* despite

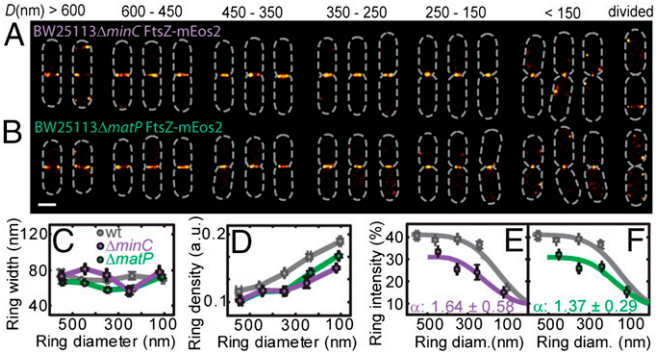

Fig. 5. Analysis of Z-ring remodeling during constriction and time-dependent septum closure rate for Δ*minC* and Δ*matP* cells. (*A* and *B*) Superresolution PALM images of live Δ*minC* (*A*) and Δ*matP* (*B*) mutants of BW25113 expressing FtsZ-mEos2, grouped by measured Z-ring diameter. Cell outlines are approximated by dashed lines. (*C*–*F*) Resolution-deconvolved ring width (*C*), density (*D*), and intensity (p_{mid}) (*E* and *F*) in Δ*minC* (purple; $n = 73$), Δ*matP* (green; $n = 68$), or wt (gray; $n = 66$) BW25113 cells expressing FtsZ-mEos2 plotted against and binned by corresponding ring diameter. Bin edges are as follows: 0, 200, 300, 400, and 500 nm. Errors bars represent SEM. Z-ring intensity measurements in *E* and *F* are overlaid with best-fit (solid line) models generated from time-lapse parameters of corresponding strain (*SI Appendix*, Table S2). Results for wt BW25113 (gray) are replicated from Fig. 3 for comparison. (Scale bar, 1 μm.)

similar alterations to Z-ring density and dynamics during the cell cycle suggests that these Z-ring properties do not limit the rate of septum closure.

Septum Closure Rate Is Correlated with Cell Elongation Rate. Thus far, our characterizations revealed that altered Z-ring GTPase activity, density, and assembly/disassembly dynamics during the cell cycle do not cause systematic changes to the rate of septum closure. This lack of a unifying, FtsZ-centric theme prompted us to explore the roles of other divisome components. We first examined the role of cell wall PG synthesis activity, which takes place in two modes during the cell cycle: initially along the lateral cell body and then predominantly septum-localized during constriction (89, 90). Septal cell wall synthesis is directed by the divisome, and lateral cell wall synthesis is directed by the 'elongasome' (91). These two systems may compete with each other, because they share the same precursors (92, 93) and/or coordinate with each other during both cell wall elongation and constriction (94–98).

To quantify PG synthesis activity during both lateral and septal cell wall synthesis, we measured cell elongation rates, calculated as cell length added per unit time, both before (v_{ep}) and during (v_{ec}) the constriction period. Under balanced growth, *E. coli* cell elongation is proportional to cell surface addition and limited by cell wall PG synthesis (99, 100). Thus, the measured v_{ep} and v_{ec} values directly reflect cell wall synthesis activity. We measured single-cell elongation rates for the two wt strains described above (BW25113 and MC4100) and two additional conditions: wt DH5α grown in M9 at RT ($\tau = 181 \pm 8$ min, $n = 40$) and the same BW25113 strain growing faster in rich defined medium (EZ-RDM) at RT ($\tau = 94 \pm 2$ min, $n = 80$). Time-lapse analyses and live-cell PALM imaging of the two additional wt strains showed similar Z-ring assembly dynamics (*SI Appendix*, Table S2), two-phase constriction (*SI Appendix*, Fig. S9), and continuous increase of Z-ring density throughout constriction (*SI Appendix*, Fig. S10). The slower growing DH5α strain exhibited lower rates for both cell elongation and septum closure compared with the BW25113 strain grown in EZ-RDM (*SI Appendix*, Table S3) but similar acceleration in septum closure rate ($\alpha = 1.4 \pm 0.4$ and 1.3 ± 0.3, respectively).

Comparison of average septum closure rates and cell elongation rates for all four wt conditions revealed that septum closure rates are highly correlated with both v_{ep} and v_{ec} ($r = 0.98$ and $r = 0.99$ and $P = 0.02$ and $P = 0.01$, respectively; Fig. 6 *A* and *B*). Interestingly, we found that the ratio v_c/v_{ec}, which compares the total diameter of the septum closed during constriction with the cell length added during that time, is close to unity for the four wt strains and conditions (Fig. 6*D*). This unity ratio can be explained by the growth of hemispherical poles in *E. coli*, in which the starting septum diameter is equivalent to the final combined length of the poles. Thus, our measurements indicate that, during constriction, cell elongation occurs predominately through septal cell wall growth, because substantial contributions from lateral growth along the cell body would result in $v_c/v_{ec} < 1$. This finding is consistent with early observations that PG incorporation activity is concentrated at the septum during the constriction period (89, 90) and highlights the method's precision in determining the elongation and septum closure rates. Collectively, these correlations suggest that the differences in septum closure rate observed in different wt strains under varying growth conditions can be attributed to differences in PG synthesis rates and that the cellular processes limiting cell wall synthesis may also limit the rate of septum closure.

Decreased Activity of PG Synthesis Enzyme FtsI Decreases Septum Closure Rate. We showed above that the rate of septum closure is highly correlated with the rate of cell wall synthesis. To further investigate whether cell wall synthesis limits the progression of septum closure, we analyzed septum closure rates in a temperature-sensitive mutant strain, MCI23, in which the total cellular activity of the essential cell wall transpeptidase, FtsI (also known as PBP3), is reduced even at permissive temperatures, likely because of decreased thermostability of the protein (101). FtsI localizes to the septum at the onset of constriction (102, 103) and exhibits stimulated transpeptidase activity in dividing cells compared with nondividing cells (104). If FtsI's PG synthesis activity, rather than Z-ring contraction, were a primary driver of septum closure, we would expect the lowered FtsI activity in the MCI23 strain to result in a reduced rate of septum closure.

We grew MCI23 under the same condition as its wt parent strain MC4100 (RT, M9 medium) and found that at this permissive condition, MCI23 had a slightly faster cell doubling time (105 ± 3 min, $n = 103$ vs. 114 ± 3 min, $n = 78$ for wt MC4100, $P = 0.03$; *SI Appendix*, Table S2). However, the corresponding mean septum closure rate measured in MCI23 ($v_c = 12.5 \pm 0.4$ nm/min) was much slower than that of the wt MC4100 ($v_c = 19.3 \pm 0.7$ nm/min, $P < 5 \times 10^{-5}$) because of a prolonged constriction period ($\tau_c = 50 \pm 2$ min, $n = 103$ vs. 32 ± 2 min, $n = 78$ for wt MC4100, $P = 8 \times 10^{-16}$). This

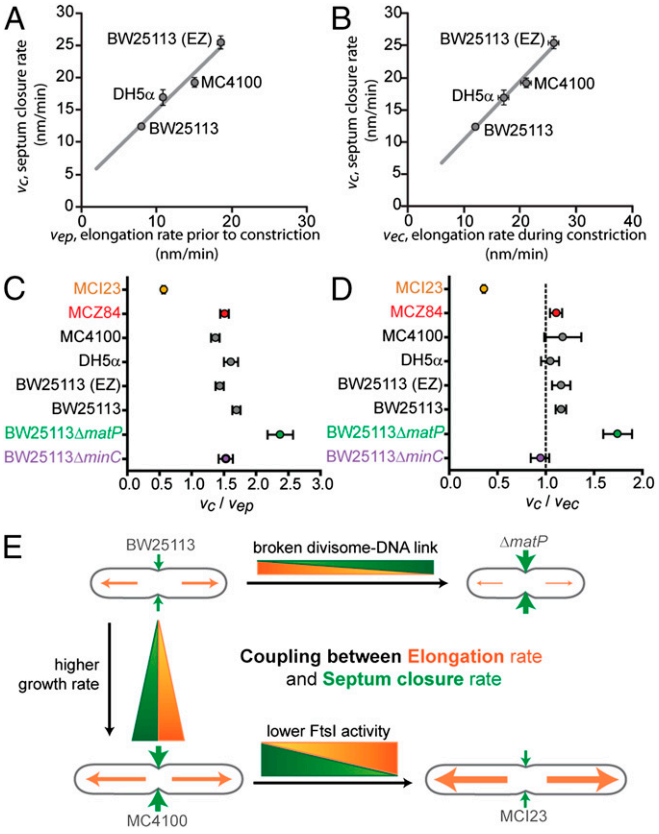

Fig. 6. Comparison of septum closure and cell elongation rates. (*A* and *B*) Average septum closure rate ($\langle v_c \rangle$) plotted against cell elongation rate before ($\langle v_{ep} \rangle$) (*A*) or during ($\langle v_{ec} \rangle$) (*B*) constriction for all wt *E. coli* strains (gray circles), with associated linear trend lines (gray lines) [trend line in *A*: $y = 1.14x + 3.75$ ($r_{Pearson} = 0.98$, $P = 0.02$); trend line in *B*: $y = 0.91x + 1.33$ ($r_{Pearson} = 0.99$, $P = 0.01$)]. (*C* and *D*) Average ratio of septum closure rate relative to cell elongation rate before ($\langle v_c/v_{ep} \rangle$) (*A*) or during ($\langle v_c/v_{ec} \rangle$) (*B*) constriction for all wt (gray) and mutant (colored) *E. coli* strains. The dotted line in *D* illustrates $\langle v_c/v_{ec} \rangle = 1$ ratio. (*E*) Schematic depicting the correlation between cell elongation rate and septum closure rate in wt cells under different growth conditions (wt BW25113 and MC4100 cells) (*Left*) and the anticorrelation between cell elongation rate and septum closure rate when the balance between cell wall synthesis and septum closure is perturbed under the same growth condition (*Upper*, Δ*matP* vs. wt BW25113 cells; *Lower*, MCI23 vs. wt MC4100 cells).

slowed septum closure rate in MCI23 suggests a rate-limiting role for FtsI activity in septum closure.

Interestingly, the cell elongation rates of MCI23 before (v_{ep} = 23.0 ± 0.6 nm/min vs. 15.0 ± 0.4 for wt MC4100, $P = 1.8 \times 10^{-26}$) and during (v_{ec} = 35.7 ± 0.7 nm/min vs. 21.2 ± 0.9 for wt MC4100, $P = 1.1 \times 10^{-20}$) constriction are significantly faster than those of the wt MC4100 strain. As a result, MCI23 cells are longer (3.17 ± 0.05 μm at birth, n = 103 vs. 1.97 ± 0.03 μm, n = 78 for wt MC4100, $P = 7 \times 10^{-46}$; *SI Appendix*, Table S3) and exhibit v_c/v_{ec} and v_c/v_{ep} ratios (septum closure rate normalized to cell elongation rate) that are substantially smaller than those of all other wt strains (Fig. 6 *C* and *D* and *SI Appendix*, Table S3). These results suggest that normal FtsI activity may inhibit lateral cell wall synthesis, which contributes most significantly to cell elongation, and that the competitive balance between lateral and septal cell wall synthesis (92, 93), if present, is shifted in the MCI23 mutant.

To investigate whether the significantly reduced septum closure rate in MCI23 could be attributable to indirect effects on Z-ring structure or dynamics, we characterized Z-ring structures observed by PALM imaging of FtsZ-mEos2 in the mutant. Z-rings in MCI23 exhibited similar clustered morphologies (*SI Appendix*, Fig. S11*A*), widths (*SI Appendix*, Table S1, Fig. S11*B*, and Fig. S3*D*), and condensation (*SI Appendix*, Fig. S11*D*) to those in the wt MC4100 strain, although Z-ring density was generally 20–30% lower than that in MC4100 (*SI Appendix*, Fig. S11*D* and Fig. S3*F*). This reduction in Z-ring density may be caused by the significantly longer length of MCI23 cells, which creates a larger non-midcell surface area for FtsZ to sample compared with that in MC4100 cells. Nonetheless, our characterizations of the Δ*minC* and Δ*matP* cells, which exhibited more substantial density reductions (Fig. 5*D*), suggest that reduced Z-ring density is not responsible for the significantly reduced septum closure rate of MCI23.

Absence of MatP Modulates the Correlation Between Cell Wall Elongation and Septum Closure Rate. Having observed a more dominant role for cell wall synthesis rather than Z-ring contraction in limiting septum closure rates, we examined whether differences in cell elongation rates could also explain the differences in septum closure rates that we observed in MCZ84, Δ*minC*, and Δ*matP* cells. We found that the relative ratios v_c/v_{el} and v_c/v_{ec} of MCZ84 and Δ*minC* cells were similar to all wt conditions measured (<20% difference; Fig. 6 *C* and *D* and *SI Appendix*, Table S3), indicating that the septum closure rates of these strains can be well explained by their respective cell wall growth rates and reinforcing the negligible roles of FtsZ GTPase activity, condensation, and assembly/disassembly dynamics in regulating septum closure rates. More interestingly, we found that the relative ratios v_c/v_{el} and v_c/v_{ec} of Δ*matP* cells were significantly larger than the wt conditions, with $\langle v_c/v_{ep} \rangle = 2.4 \pm 0.2$ (vs. 1.7 ± 0.1 for wt BW25113 in M9, $P = 2.5 \times e^{-4}$) and $\langle v_c/v_{ec} \rangle = 1.8 \pm 0.2$ (vs. 1.2 ± 0.1 for wt BW25113 in M9, $P < 5 \times e^{-5}$), respectively (Fig. 6 *C* and *D* and *SI Appendix*, Table S3). Thus, septum closure rates in Δ*matP* cells are faster than that expected given their cell elongation rates, supporting a model in which a MatP-related process can modulate the coupling between cell wall PG synthesis and the progress of septum closure (18).

Independent Septum Closure Rate Measurements Support Fluorescence Measurements. Our integrated measurement of septum closure rate is based on superresolution imaging, which provides the most accurate measurement of septum diameter, and fluorescence time-lapse imaging, which enables reliable measurement of the constriction period, τ_c, by the final departure of FtsZ-GFP fluorescence from midcell. To determine whether the use of FtsZ fluorescent fusion proteins influences these measurements, we performed analogous experiments on the background strains devoid of fluorescent fusions. We measured the diameter at constriction initiation by either immuno-superresolution imaging (105) on cells labeled with Alexa647-conjugated wheat germ agglutinin (WGA) (106, 107) or by segmenting phase-contrast cell images using the MicrobeTracker software (108) (*SI Appendix*, Fig. S8 *A*–*C*). These two diameter measurements correlate with each other and are both consistently larger than the corresponding septum diameter measured using FtsZ-mEos2, which is consistent with WGA binding to the cell periphery (106), whereas FtsZ-mEos2 resides inside of the inner membrane. To measure the constriction period τ_c, we performed time-lapse phase-contrast imaging of cells growing on a microscope stage and used the MicrobeTracker software and custom fitting routines to determine when the constriction period ends (*SI Appendix*, Fig. S8*D* and Table S4). The latter analysis proved difficult and highly variable as diffraction-limited bright field imaging caused diameter reductions below ∼500 nm to be indiscernible (*SI Appendix*, Fig. S8*D*). Consequently, we were not able to determine when the constriction period ends with confidence but rather used a characteristic time between the frame when the diameter was first reduced by 10% of the discernible range to the frame when it had been reduced by 90% of the range (i.e., from ∼900 to ∼600 nm) as a proxy. Note that the use of this pseudo-constriction period appeared to reduce the differences between all mutant and wt strains (*SI Appendix*, Fig. S8*D*) compared with the original measurements (Fig. 6*D*). This reduced effect is likely attributable to larger measurement uncertainties in diffraction-limited imaging, because the same analysis applied to FtsZ-GFP–expressing BW25113 strains (wt, Δ*matP*, and Δ*minC*) resulted in similar observations. Nevertheless, the *ftsI23* mutation still showed a significantly larger effect on the cell elongation rate-adjusted septum closure rate (v_c/v_{ec}) than any other FtsZ-related mutations (Fig. 6*D* and *SI Appendix*, Fig. S8*E*). These results thus support our major conclusion that septum closure is likely driven by septum synthesis rather than Z-ring contraction.

Discussion

In this work, we illustrated the 3D structural organization and remodeling of the Z-ring during constriction with unprecedented resolution. We demonstrated that the *E. coli* Z-ring is composed of discontinuous FtsZ clusters loosely confined to a toroidal zone of ∼100-nm width and ∼60-nm thickness. Because the mean Z-ring thickness is significantly larger than that of a single layer of FtsZ protofilaments, the Z-ring can most likely accommodate multiple layers of FtsZ protofilaments along the radial direction, consistent with previous predictions (48, 59). Although our resolution could not resolve the number or orientations of individual FtsZ protofilaments within FtsZ clusters, the small cluster size observed (<100 nm in all directions; Fig. 1*C* and *SI Appendix*, Fig. S4) supports heterogeneity in FtsZ protofilament orientation (67), because the membrane curvature preference of short ∼50-nm protofilaments was estimated to be only ∼0.1 k_BT (109).

We note that, in vitro, membrane-attached FtsZ can form long, continuous protofilaments (33, 35) and that a recent ECT study observed long, single-layered protofilaments at cell division sites (35). These studies support a smooth, continuous Z-ring organization. However, Z-ring discontinuity has been observed in many bacterial species (19, 37, 48, 51–54), and incomplete Z-rings have been shown to lead to cell wall indentation (110), suggesting that ring completion is not required for Z-ring function. We suggest that the continuous and discontinuous organizations reflect different dynamic states of the Z-ring modulated by FtsZ's GTPase activity, which is known to promote the fracture of long FtsZ polymers (111) and to modulate FtsZ turnover dynamics (82). Active GTP hydrolysis may thus serve to constantly remodel the Z-ring, generating a discontinuous, clustered organization that can reorganize promptly in response to cellular cues. This GTPase-dependent remodeling may explain why long

FtsZ protofilaments were more apparent with an overexpressed FtsZ variant with low GTPase activity (D212A) (35).

What is the role of the Z-ring during cytokinesis? As a large body of work has already demonstrated, the Z-ring is an essential scaffold that recruits all other division proteins to initiate cell wall constriction (2). FtsZ has also been implicated in preseptal cell wall synthesis that occurs before the onset of constriction (97, 112). The force-generating function and mechanisms of the Z-ring, however, have been highly debated (113). We reasoned that if the Z-ring actively generates a force to invaginate the inner membrane, which is then followed by septal cell wall growth, then perturbing various Z-ring properties and observing the consequences on septum closure rates would allow us to characterize its force generation mechanism. However, these perturbations, summarized below, consistently supported a model in which the Z-ring does not play a rate-limiting role in septum closure.

First, we found that septum closure is not limited by FtsZ's GTPase activity, because the *ftsz84* mutant showed essentially the same septum closure rate as its wt parent strain. Second, we found that septum closure is not coupled to Z-ring disassembly because cell wall constriction initiated significantly earlier than Z-ring disassembly under all conditions (*SI Appendix*, Table S2) and because the diameter at which individual Z-rings started to disassemble varied widely (from 600 to 250 nm) among different conditions (Figs. 4 *E* and *F* and 5 *E* and *F* and *SI Appendix*, Fig. S10*B*). Third, we found that septum closure is not driven by Z-ring density (FtsZ concentration in the ring) because reduced density in the Δ*minC*, Δ*matP*, and MCI23 strains led to both increases and decreases in septum closure rate, and increased density in the *ftsz84* mutant strain did not alter septum closure rate. The Z-ring indeed condenses during the constriction period as previously proposed (35, 38, 42, 43); however, this condensation may be a natural consequence of Z-ring remodeling in response to the gradually reducing septum diameter. Fourth, we found that septum closure cannot be coupled to FtsZ's assembly dynamics during the cell cycle, because three mutations (*ftsz84*, Δ*minC*, and Δ*matP*) resulted in delayed Z-ring stabilization at midcell but did not lead to systematic changes in the septum closure rate. Collectively, these results indicate that the Z-ring does not limit the rate of septum closure under the range of conditions tested here.

Although Z-ring perturbations showed no clear influence on septum closure rate, we did observe a strong correlation between septum closure rate and cell elongation rate in wt, *ftsZ84*, and Δ*minC* cells (Fig. 6 *A* and *B* and *SI Appendix*, Table S3). These observations suggest that cell wall synthesis activity, rather than Z-ring contraction, plays a limiting role in the progress of septum closure. Supporting this limiting role, we observed a significantly slowed septum closure rate in the presence of diminished septal transpeptidase activity by FtsI (MCI23 strain). We note that early studies have reported prolonged constriction periods caused by mutations in FtsI or FtsQ (114–116) or by overexpression of FtsN (116), although the corresponding cell wall synthesis activity was not assessed; these proteins are all essential components of the divisome involved in septal cell wall synthesis (117). Interestingly, recent work has shown that cytokinesis in fission yeast is primarily driven by cell wall synthesis rather than contraction of the force-generating actomyosin ring (118), suggesting that some similarities may exist in the mechanisms adapted by different kingdoms of life to coordinate cytokinesis in walled cells.

Our study also sheds light on another important factor that can influence the rate of septum closure: coordination between septum closure and chromosome segregation. We found that the absence of MatP modulated the correlation between septum closure and cell elongation during cytokinesis, as measured by the ratio of septum closure to cell elongation rate (Fig. 6 *C* and *D*). MatP promotes condensation of the *ter* region of the chromosome by binding to *ter*-localized *matS* sites (17) and connects the divisome to the chromosome via the FtsZ-ZapA-ZapB-MatP network (18). In the absence of MatP, mobility of the *ter* region increases and sister *ter* foci prematurely separate (16, 17, 21). With fast growth, deletion of *matP* causes additional defects in chromosome segregation and Z-ring morphology that are not apparent under slow growth ($\tau > 60$ min) (17, 19). Given that the experiments presented here were carried out in slow-growth conditions, the increase in septum closure rate we observed in the *matP* deletion strain is most likely caused by the broken FtsZ-ZapA-ZapB-MatP linkage and/or the early displacement of *ter* DNA from the division plane rather than chromosome segregation defects or changes in Z-ring structures. An intact FtsZ-ZapA-ZapB-MatP linkage and midcell colocalized *ter* DNA may normally function as braking/sensing mechanisms that physically or biochemically impede inward septum growth to avoid premature septum closure over unsegregated chromosomes.

An additional interesting observation is that in the two mutant strains, MCI23 and Δ*matP*, the correlation between lateral cell elongation rate and septum closure rate observed in wt strains is not only broken but also appears to be anticorrelated. MCI23 cells have slower septum closure rates but much faster cell elongation rates compared with wt MC4100 cells, whereas Δ*matP* cells exhibit the opposite changes relative to wt BW25113 cells (*SI Appendix*, Table S3). These anticorrelated effects support a model in which lateral and septal cell wall synthesis may compete for a constant pool of enzymes or PG precursors, the level of which is determined by the growth condition (92, 93). The positive correlation between septum closure and elongation rates that we observed for wt cells (Fig. 6 *A* and *B*) could thus be explained by the effect of precursor or enzyme levels on total cell wall synthesis rates, which is partitioned between lateral and septal growth. When the competitive balance between these two processes is unperturbed, their rates both scale with total cell wall synthesis rates (Fig. 6*E*, *Left*), but when the balance is altered, as in the Δ*matP* or MCI23 strains, the processes exhibit opposing changes in rate (Fig. 6*E*, *Upper* or *Lower*). The exact mechanisms by which septal and lateral cell wall synthesis rates are coregulated remain unknown, but these observations clearly indicate that the rate of septum closure is highly influenced by cell wall synthesis.

Our results do not exclude the existence of a FtsZ-generated constrictive force but rather indicate that such a force is not rate-limiting for septum closure. A non–rate-limiting FtsZ-generated force may serve primarily to direct the spatial and temporal activity of other divisome constituents rather than to pull the cytoplasmic membrane actively to drive envelope constriction. A recent computational modeling study showed that a substantial force (>400 pN) would be needed to constrict a static *E. coli* cell wall but that the existence of cell wall turnover and remodeling can reduce the required constrictive force to as little as ∼8 pN, which can be provided by the Z-ring (119). This small Z-ring contribution relative to that of cell wall remodeling is consistent with the estimated 20–90 pN of force generated by FtsZ filaments reconstituted on liposomes (45, 120) and our finding that cell wall synthesis has a larger influence on the rate of septum closure than does Z-ring contraction. However, this modeling study predicts that the rate of septum closure should be proportional to the amount of constrictive force generated by the Z-ring (119). This prediction can only be consistent with our findings if the mechanism of Z-ring force generation is not driven by any of the properties perturbed here (GTPase activity, density, assembly/disassembly dynamics) or if the source of the constrictive force is not the Z-ring.

To summarize, our findings support a model in which the roles of cell wall synthesis and chromosome segregation dominate that of the Z-ring in defining the rate of septum closure during

constriction in *E. coli*. These results challenge a FtsZ-centric view of cytokinesis in bacteria and suggest that FtsZ should be viewed as a key structural scaffold, regulator, or mediator rather than as a major force generator.

Materials and Methods

All strains and plasmids used in this study, their construction, growth conditions, and expression characterizations are described in *SI Appendix, Supplemental Experimental Procedures*. Imaging and analysis conditions used for all superresolution and time-lapse microscopy experiments are also described in *SI Appendix, Supplemental Experimental Procedures*. All reported errors are SEMs unless otherwise noted. All reported correlation values are Pearson's *r*. Two-tailed *P* values for comparison of structural dimensions and time-lapse period durations were calculated using Student's *t*. Two-tailed *P* values for comparison of septum closure rates (v_c) and rate ratios ($\langle v_c/v_{ep}\rangle$ and $\langle v_c/v_{ec}\rangle$) were calculated using randomization tests with 20,000 iterations.

ACKNOWLEDGMENTS. We thank Dr. Harald Hess and Dr. Gleb Shtengel for technical guidance and for use of their iPALM instrumentation at the HHMI Janelia Farm Research Campus. We also thank Dr. Jon Beckwith, Dr. Harold Erickson, Dr. Tao Huang, Dr. Xinxing Yang, and the *E. coli* Genetic Stock Center at Yale University for strains, plasmids, and antibodies. This study was supported by National Institutes of Health Grant 1R01GM086447-01A2 and National Science Foundation Grant EAGER MCB1019000.

1. Sass P, Brötz-Oesterhelt H (2013) Bacterial cell division as a target for new antibiotics. *Curr Opin Microbiol* 16(5):522–530.
2. Adams DW, Errington J (2009) Bacterial cell division: Assembly, maintenance and disassembly of the Z ring. *Nat Rev Microbiol* 7(9):642–653.
3. de Boer P, Crossley R, Rothfield L (1992) The essential bacterial cell-division protein FtsZ is a GTPase. *Nature* 359(6392):254–256.
4. RayChaudhuri D, Park JT (1992) Escherichia coli cell-division gene ftsZ encodes a novel GTP-binding protein. *Nature* 359(6392):251–254.
5. Pichoff S, Lutkenhaus J (2005) Tethering the Z ring to the membrane through a conserved membrane targeting sequence in FtsA. *Mol Microbiol* 55(6):1722–1734.
6. Hale CA, de Boer PA (1997) Direct binding of FtsZ to ZipA, an essential component of the septal ring structure that mediates cell division in E. coli. *Cell* 88(2):175–185.
7. Bi EF, Lutkenhaus J (1991) FtsZ ring structure associated with division in Escherichia coli. *Nature* 354(6349):161–164.
8. Goehring NW, Beckwith J (2005) Diverse paths to midcell: Assembly of the bacterial cell division machinery. *Curr Biol* 15(13):R514–R526.
9. Typas A, Banzhaf M, Gross CA, Vollmer W (2012) From the regulation of peptidoglycan synthesis to bacterial growth and morphology. *Nat Rev Microbiol* 10(2):123–136.
10. Small E, et al. (2007) FtsZ polymer-bundling by the Escherichia coli ZapA orthologue, YgfE, involves a conformational change in bound GTP. *J Mol Biol* 369(1):210–221.
11. Galli E, Gerdes K (2012) FtsZ-ZapA-ZapB interactome of Escherichia coli. *J Bacteriol* 194(2):292–302.
12. Durand-Heredia JM, Yu HH, De Carlo S, Lesser CF, Janakiraman A (2011) Identification and characterization of ZapC, a stabilizer of the FtsZ ring in Escherichia coli. *J Bacteriol* 193(6):1405–1413.
13. Hale CA, et al. (2011) Identification of Escherichia coli ZapC (YcbW) as a component of the division apparatus that binds and bundles FtsZ polymers. *J Bacteriol* 193(6):1393–1404.
14. Durand-Heredia J, Rivkin E, Fan G, Morales J, Janakiraman A (2012) Identification of ZapD as a cell division factor that promotes the assembly of FtsZ in Escherichia coli. *J Bacteriol* 194(12):3189–3198.
15. Marteyn BS, et al. (2014) ZapE is a novel cell division protein interacting with FtsZ and modulating the Z-ring dynamics. *MBio* 5(2):e00022-14.
16. Espéli O, et al. (2012) A MatP-divisome interaction coordinates chromosome segregation with cell division in E. coli. *EMBO J* 31(14):3198–3211.
17. Mercier R, et al. (2008) The MatP/matS site-specific system organizes the terminus region of the E. coli chromosome into a macrodomain. *Cell* 135(3):475–485.
18. Buss J, et al. (2015) A multi-layered protein network stabilizes the Escherichia coli FtsZ-ring and modulates constriction dynamics. *PLoS Genet* 11(4):e1005128.
19. Buss J, et al. (2013) In vivo organization of the FtsZ-ring by ZapA and ZapB revealed by quantitative super-resolution microscopy. *Mol Microbiol* 89(6):1099–1120.
20. Deghorain M, et al. (2011) A defined terminal region of the E. coli chromosome shows late segregation and high FtsK activity. *PLoS One* 6(7):e22164.
21. Stouf M, Meile JC, Cornet F (2013) FtsK actively segregates sister chromosomes in Escherichia coli. *Proc Natl Acad Sci USA* 110(27):11157–11162.
22. Yu XC, Weihe EK, Margolin W (1998) Role of the C terminus of FtsK in Escherichia coli chromosome segregation. *J Bacteriol* 180(23):6424–6428.
23. Steiner W, Liu G, Donachie WD, Kuempel P (1999) The cytoplasmic domain of FtsK protein is required for resolution of chromosome dimers. *Mol Microbiol* 31(2):579–583.
24. Li Y, Youngren B, Sergueev K, Austin S (2003) Segregation of the Escherichia coli chromosome terminus. *Mol Microbiol* 50(3):825–834.
25. Liu G, Draper GC, Donachie WD (1998) FtsK is a bifunctional protein involved in cell division and chromosome localization in Escherichia coli. *Mol Microbiol* 29(3):893–903.
26. Bailey MW, Bisicchia P, Warren BT, Sherratt DJ, Männik J (2014) Evidence for divisome localization mechanisms independent of the Min system and SlmA in Escherichia coli. *PLoS Genet* 10(8):e1004504.
27. Meier EL, Goley ED (2014) Form and function of the bacterial cytokinetic ring. *Curr Opin Cell Biol* 26:19–27.
28. Erickson HP, Anderson DE, Osawa M (2010) FtsZ in bacterial cytokinesis: Cytoskeleton and force generator all in one. *Microbiol Mol Biol Rev* 74(4):504–528.
29. Nanninga N (1998) Morphogenesis of Escherichia coli. *Microbiol Mol Biol Rev* 62(1):110–129.
30. Osawa M, Anderson DE, Erickson HP (2008) Reconstitution of contractile FtsZ rings in liposomes. *Science* 320(5877):792–794.
31. Osawa M, Anderson DE, Erickson HP (2009) Curved FtsZ protofilaments generate bending forces on liposome membranes. *EMBO J* 28(22):3476–3484.
32. Osawa M, Erickson HP (2011) Inside-out Z rings–Constriction with and without GTP hydrolysis. *Mol Microbiol* 81(2):571–579.
33. Milam SL, Osawa M, Erickson HP (2012) Negative-stain electron microscopy of inside-out FtsZ rings reconstituted on artificial membrane tubules show ribbons of protofilaments. *Biophys J* 103(1):59–68.
34. Osawa M, Erickson HP (2013) Liposome division by a simple bacterial division machinery. *Proc Natl Acad Sci USA* 110(27):11000–11004.
35. Szwedziak P, Wang Q, Bharat TAM, Tsim M, Löwe J (2014) Architecture of the ring formed by the tubulin homologue FtsZ in bacterial cell division. *Elife* 3:e04601.
36. Lu C, Reedy M, Erickson HP (2000) Straight and curved conformations of FtsZ are regulated by GTP hydrolysis. *J Bacteriol* 182(1):164–170.
37. Li Z, Trimble MJ, Brun YV, Jensen GJ (2007) The structure of FtsZ filaments in vivo suggests a force-generating role in cell division. *EMBO J* 26(22):4694–4708.
38. Ghosh B, Sain A (2008) Origin of contractile force during cell division of bacteria. *Phys Rev Lett* 101(17):178101.
39. Allard JF, Cytrynbaum EN (2009) Force generation by a dynamic Z-ring in Escherichia coli cell division. *Proc Natl Acad Sci USA* 106(1):145–150.
40. Chen Y, Erickson HP (2011) Conformational changes of FtsZ reported by tryptophan mutants. *Biochemistry* 50(21):4675–4684.
41. Li Y, et al. (2013) FtsZ protofilaments use a hinge-opening mechanism for constrictive force generation. *Science* 341(6144):392–395.
42. Surovtsev IV, Morgan JJ, Lindahl PA (2008) Kinetic modeling of the assembly, dynamic steady state, and contraction of the FtsZ ring in prokaryotic cytokinesis. *PLOS Comput Biol* 4(7):e1000102.
43. Lan G, Daniels BR, Dobrowsky TM, Wirtz D, Sun SX (2009) Condensation of FtsZ filaments can drive bacterial cell division. *Proc Natl Acad Sci USA* 106(1):121–126.
44. Hörger I, et al. (2008) Langevin computer simulations of bacterial protein filaments and the force-generating mechanism during cell division. *Phys Rev E Stat Nonlin Soft Matter Phys* 77(1 Pt 1):011902.
45. Paez A, et al. (2009) Simple modeling of FtsZ polymers on flat and curved surfaces: Correlation with experimental in vitro observations. *PMC Biophys* 2(1):8.
46. Ghosh B, Sain A (2011) Force generation in bacteria without nucleotide-dependent bending of cytoskeletal filaments. *Phys Rev E Stat Nonlin Soft Matter Phys* 83(5 Pt 1):051924.
47. Betzig E, et al. (2006) Imaging intracellular fluorescent proteins at nanometer resolution. *Science* 313(5793):1642–1645.
48. Fu G, et al. (2010) In vivo structure of the E. coli FtsZ-ring revealed by photoactivated localization microscopy (PALM). *PLoS One* 5(9):e12682.
49. Coltharp C, Kessler RP, Xiao J (2012) Accurate construction of photoactivated localization microscopy (PALM) images for quantitative measurements. *PLoS One* 7(12):e51725.
50. Buss J, Coltharp C, Xiao J (2013) Super-resolution imaging of the bacterial division machinery. *J Vis Exp* 71:e50048.
51. Strauss MP, et al. (2012) 3D-SIM super resolution microscopy reveals a bead-like arrangement for FtsZ and the division machinery: Implications for triggering cytokinesis. *PLoS Biol* 10(9):e1001389.
52. Leisch N, et al. (2012) Growth in width and FtsZ ring longitudinal positioning in a gammaproteobacterial symbiont. *Curr Biol* 22(19):R831–R832.
53. Holden SJ, et al. (2014) High throughput 3D super-resolution microscopy reveals Caulobacter crescentus in vivo Z-ring organization. *Proc Natl Acad Sci USA* 111(12):4566–4571.
54. Rowlett VW, Margolin W (2014) 3D-SIM super-resolution of FtsZ and its membrane tethers in Escherichia coli cells. *Biophys J* 107(8):L17–L20.
55. Shtengel G, et al. (2009) Interferometric fluorescent super-resolution microscopy resolves 3D cellular ultrastructure. *Proc Natl Acad Sci USA* 106(9):3125–3130.
56. Klein T, Proppert S, Sauer M (2014) Eight years of single-molecule localization microscopy. *Histochem Cell Biol* 141(6):561–575.
57. Thanedar S, Margolin W (2004) FtsZ exhibits rapid movement and oscillation waves in helix-like patterns in Escherichia coli. *Curr Biol* 14(13):1167–1173.
58. Niu L, Yu J (2008) Investigating intracellular dynamics of FtsZ cytoskeleton with photoactivation single-molecule tracking. *Biophys J* 95(4):2009–2016.
59. Carmon G, Fishov I, Feingold M (2012) Oriented imaging of 3D subcellular structures in bacterial cells using optical tweezers. *Opt Lett* 37(3):440–442.
60. Biteen JS, Goley ED, Shapiro L, Moerner WE (2012) Three-dimensional super-resolution imaging of the midplane protein FtsZ in live Caulobacter crescentus cells using astigmatism. *Chemphyschem* 13(4):1007–1012.

61. Coltharp C, Yang X, Xiao J (2014) Quantitative analysis of single-molecule superresolution images. *Curr Opin Struct Biol* 28:112–121.
62. Veatch SL, et al. (2012) Correlation functions quantify super-resolution images and estimate apparent clustering due to over-counting. *PLoS One* 7(2):e31457.
63. Sengupta P, Jovanovic-Talisman T, Lippincott-Schwartz J (2013) Quantifying spatial organization in point-localization superresolution images using pair correlation analysis. *Nat Protoc* 8(2):345–354.
64. Romberg L, Simon M, Erickson HP (2001) Polymerization of Ftsz, a bacterial homolog of tubulin. is assembly cooperative? *J Biol Chem* 276(15):11743–11753.
65. Chen Y, Bjornson K, Redick SD, Erickson HP (2005) A rapid fluorescence assay for FtsZ assembly indicates cooperative assembly with a dimer nucleus. *Biophys J* 88(1): 505–514.
66. Huecas S, et al. (2008) Energetics and geometry of FtsZ polymers: Nucleated self-assembly of single protofilaments. *Biophys J* 94(5):1796–1806.
67. Si F, Busiek K, Margolin W, Sun SX (2013) Organization of FtsZ filaments in the bacterial division ring measured from polarized fluorescence microscopy. *Biophys J* 105(9):1976–1986.
68. Dajkovic A, Pichoff S, Lutkenhaus J, Wirtz D (2010) Cross-linking FtsZ polymers into coherent Z rings. *Mol Microbiol* 78(3):651–668.
69. Monahan LG, Robinson A, Harry EJ (2009) Lateral FtsZ association and the assembly of the cytokinetic Z ring in bacteria. *Mol Microbiol* 74(4):1004–1017.
70. Peters NT, Dinh T, Bernhardt TG (2011) A fail-safe mechanism in the septal ring assembly pathway generated by the sequential recruitment of cell separation amidases and their activators. *J Bacteriol* 193(18):4973–4983.
71. Anderson DE, Gueiros-Filho FJ, Erickson HP (2004) Assembly dynamics of FtsZ rings in Bacillus subtilis and Escherichia coli and effects of FtsZ-regulating proteins. *J Bacteriol* 186(17):5775–5781.
72. Geissler B, Shiomi D, Margolin W (2007) The ftsA* gain-of-function allele of Escherichia coli and its effects on the stability and dynamics of the Z ring. *Microbiology* 153(Pt 3):814–825.
73. Rueda S, Vicente M, Mingorance J (2003) Concentration and assembly of the division ring proteins FtsZ, FtsA, and ZipA during the Escherichia coli cell cycle. *J Bacteriol* 185(11):3344–3351.
74. Weart RB, Levin PA (2003) Growth rate-dependent regulation of medial FtsZ ring formation. *J Bacteriol* 185(9):2826–2834.
75. Tsukanov R, et al. (2011) Timing of Z-ring localization in Escherichia coli. *Phys Biol* 8(6):066003.
76. Inoue I, Ino R, Nishimura A (2009) New model for assembly dynamics of bacterial tubulin in relation to the stages of DNA replication. *Genes Cells* 14(3):435–444.
77. Reshes G, Vanounou S, Fishov I, Feingold M (2008) Cell shape dynamics in Escherichia coli. *Biophys J* 94(1):251–264.
78. Reshes G, Vanounou S, Fishov I, Feingold M (2008) Timing the start of division in E. coli: A single-cell study. *Phys Biol* 5(4):046001.
79. Strömqvist J, Skoog K, Daley DO, Widengren J, von Heijne G (2010) Estimating Z-ring radius and contraction in dividing Escherichia coli. *Mol Microbiol* 76(1):151–158.
80. Dai K, Xu Y, Lutkenhaus J (1993) Cloning and characterization of ftsN, an essential cell division gene in Escherichia coli isolated as a multicopy suppressor of ftsA12(Ts). *J Bacteriol* 175(12):3790–3797.
81. Bi E, Lutkenhaus J (1990) Analysis of ftsZ mutations that confer resistance to the cell division inhibitor SulA (SfiA). *J Bacteriol* 172(10):5602–5609.
82. Stricker J, Maddox P, Salmon ED, Erickson HP (2002) Rapid assembly dynamics of the Escherichia coli FtsZ-ring demonstrated by fluorescence recovery after photobleaching. *Proc Natl Acad Sci USA* 99(5):3171–3175.
83. Hu Z, Lutkenhaus J (2000) Analysis of MinC reveals two independent domains involved in interaction with MinD and FtsZ. *J Bacteriol* 182(14):3965–3971.
84. Raskin DM, de Boer PA (1999) MinDE-dependent pole-to-pole oscillation of division inhibitor MinC in Escherichia coli. *J Bacteriol* 181(20):6419–6424.
85. Shen B, Lutkenhaus J (2010) Examination of the interaction between FtsZ and MinCN in E. coli suggests how MinC disrupts Z rings. *Mol Microbiol* 75(5):1285–1298.
86. Dajkovic A, Lan G, Sun SX, Wirtz D, Lutkenhaus J (2008) MinC spatially controls bacterial cytokinesis by antagonizing the scaffolding function of FtsZ. *Curr Biol* 18(4): 235–244.
87. Shiomi D, Margolin W (2007) The C-terminal domain of MinC inhibits assembly of the Z ring in Escherichia coli. *J Bacteriol* 189(1):236–243.
88. Guberman JM, Fay A, Dworkin J, Wingreen NS, Gitai Z (2008) PSICIC: Noise and asymmetry in bacterial division revealed by computational image analysis at subpixel resolution. *PLOS Comput Biol* 4(11):e1000233.
89. Wientjes FB, Nanninga N (1989) Rate and topography of peptidoglycan synthesis during cell division in Escherichia coli: Concept of a leading edge. *J Bacteriol* 171(6): 3412–3419.
90. Woldringh CL, Huls P, Pas E, Brakenhoff GJ, Nanninga N (1987) Topography of peptidoglycan synthesis during elongation and polar cap formation in a cell division mutant of Escherichia coli MC4100. *J Gen Microbiol* 133(3):575–586.
91. Szwedziak P, Löwe J (2013) Do the divisome and elongasome share a common evolutionary past? *Curr Opin Microbiol* 16(6):745–751.
92. Begg KJ, et al. (1990) The balance between different peptidoglycan precursors determines whether Escherichia coli cells will elongate or divide. *J Bacteriol* 172(12): 6697–6703.
93. Lleo MM, Canepari P, Satta G (1990) Bacterial cell shape regulation: Testing of additional predictions unique to the two-competing-sites model for peptidoglycan assembly and isolation of conditional rod-shaped mutants from some wild-type cocci. *J Bacteriol* 172(7):3758–3771.
94. Fenton AK, Gerdes K (2013) Direct interaction of FtsZ and MreB is required for septum synthesis and cell division in Escherichia coli. *EMBO J* 32(13):1953–1965.
95. Banzhaf M, et al. (2012) Cooperativity of peptidoglycan synthases active in bacterial cell elongation. *Mol Microbiol* 85(1):179–194.
96. Den Blaauwen T, Aarsman ME, Vischer NO, Nanninga N (2003) Penicillin-binding protein PBP2 of Escherichia coli localizes preferentially in the lateral wall and at mid-cell in comparison with the old cell pole. *Mol Microbiol* 47(2):539–547.
97. de Pedro MA, Quintela JC, Höltje JV, Schwarz H (1997) Murein segregation in Escherichia coli. *J Bacteriol* 179(9):2823–2834.
98. Varma A, de Pedro MA, Young KD (2007) FtsZ directs a second mode of peptidoglycan synthesis in Escherichia coli. *J Bacteriol* 189(15):5692–5704.
99. Rojas E, Theriot JA, Huang KC (2014) Response of Escherichia coli growth rate to osmotic shock. *Proc Natl Acad Sci USA* 111(21):7807–7812.
100. Lee TK, et al. (2014) A dynamically assembled cell wall synthesis machinery buffers cell growth. *Proc Natl Acad Sci USA* 111(12):4554–4559.
101. Begg KJ, Spratt BG, Donachie WD (1986) Interaction between membrane proteins PBP3 and rodA is required for normal cell shape and division in Escherichia coli. *J Bacteriol* 167(3):1004–1008.
102. Wang L, Khattar MK, Donachie WD, Lutkenhaus J (1998) FtsI and FtsW are localized to the septum in Escherichia coli. *J Bacteriol* 180(11):2810–2816.
103. Weiss DS, et al. (1997) Localization of the Escherichia coli cell division protein FtsI (PBP3) to the division site and cell pole. *Mol Microbiol* 25(4):671–681.
104. Eberhardt C, Kuerschner L, Weiss DS (2003) Probing the catalytic activity of a cell division-specific transpeptidase in vivo with beta-lactams. *J Bacteriol* 185(13): 3726–3734.
105. Rust MJ, Bates M, Zhuang X (2006) Sub-diffraction-limit imaging by stochastic optical reconstruction microscopy (STORM). *Nat Methods* 3(10):793–795.
106. Ursell TS, et al. (2014) Rod-like bacterial shape is maintained by feedback between cell curvature and cytoskeletal localization. *Proc Natl Acad Sci USA* 111(11): E1025–E1034.
107. Lotan R, Sharon N, Mirelman D (1975) Interaction of wheat-germ agglutinin with bacterial cells and cell-wall polymers. *Eur J Biochem* 55(1):257–262.
108. Sliusarenko O, Heinritz J, Emonet T, Jacobs-Wagner C (2011) High-throughput, subpixel precision analysis of bacterial morphogenesis and intracellular spatio-temporal dynamics. *Mol Microbiol* 80(3):612–627.
109. Sun SX, Jiang H (2011) Physics of bacterial morphogenesis. *Microbiol Mol Biol Rev* 75(4):543–565.
110. Addinall SG, Lutkenhaus J (1996) FtsZ-spirals and -arcs determine the shape of the invaginating septa in some mutants of Escherichia coli. *Mol Microbiol* 22(2):231–237.
111. Mateos-Gil P, et al. (2012) Depolymerization dynamics of individual filaments of bacterial cytoskeletal protein FtsZ. *Proc Natl Acad Sci USA* 109(21):8133–8138.
112. Potluri LP, Kannan S, Young KD (2012) ZipA is required for FtsZ-dependent preseptal peptidoglycan synthesis prior to invagination during cell division. *J Bacteriol* 194(19): 5334–5342.
113. Erickson HP (2009) Modeling the physics of FtsZ assembly and force generation. *Proc Natl Acad Sci USA* 106(23):9238–9243.
114. Taschner PE, Huls PG, Pas E, Woldringh CL (1988) Division behavior and shape changes in isogenic ftsZ, ftsQ, ftsA, pbpB, and ftsE cell division mutants of Escherichia coli during temperature shift experiments. *J Bacteriol* 170(4):1533–1540.
115. Huls PG, Vischer NO, Woldringh CL (1999) Delayed nucleoid segregation in Escherichia coli. *Mol Microbiol* 33(5):959–970.
116. Aarsman ME, et al. (2005) Maturation of the Escherichia coli divisome occurs in two steps. *Mol Microbiol* 55(6):1631–1645.
117. Egan AJF, Vollmer W (2013) The physiology of bacterial cell division. *Ann N Y Acad Sci* 1277(1):8–28.
118. Proctor SA, Minc N, Boudaoud A, Chang F (2012) Contributions of turgor pressure, the contractile ring, and septum assembly to forces in cytokinesis in fission yeast. *Curr Biol* 22(17):1601–1608.
119. Lan G, Wolgemuth CW, Sun SX (2007) Z-ring force and cell shape during division in rod-like bacteria. *Proc Natl Acad Sci USA* 104(41):16110–16115.
120. Hörger I, Campelo F, Hernández-Machado A, Tarazona P (2010) Constricting force of filamentary protein rings evaluated from experimental results. *Phys Rev E Stat Nonlin Soft Matter Phys* 81(3 Pt 1):031922.